7250 *Macromolecules* **2010**, *43*, 7250–7260
DOI: 10.1021/ma1008308

Macromolecules
ARTICLE

Probing Relief Terraces in Destabilized Thin Films of an Asymmetric Block Copolymer with Grazing-Incidence Small-Angle X-ray Scattering

Ya-Sen Sun,* Shih-Wei Chien, and Jiun-You Liou

Department of Chemical and Materials Engineering, National Central University, Taoyuan 32001, Taiwan

Received April 15, 2010; Revised Manuscript Received May 12, 2010

ABSTRACT: X-ray scattering in a grazing-incidence geometry (GISAXS) was used to study relief microstructures in thin films of asymmetric polystyrene-*block*-poly(methyl methacrylate) P(S-*b*-MMA) that dewetted on SiO_x/Si and PMMA−SiO_x/Si after isothermal annealing at 210 °C for 12 h. The micro- and nanostructures of a P(S-*b*-MMA) film deposited on PS−SiO_x/Si were studied for comparison. The diffuse scattering streaks observed at angles with respect to the film normal direction in the GISAXS patterns correlate with the formation of relief terraces comprising parallel PMMA cylinders packed within a PS matrix. The relief terraces reveal a facet-like wedge at the edge, resulting from partial wetting of the nonanchored P(S-*b*-MMA) top layer at contact angles in the range 4−6.5° on a monolayer of autophobic P(S-*b*-MMA) brushes anchored onto SiO_x/Si and PMMA−SiO_x/Si.

Introduction

Dewetting of thin films of block copolymers (BCP) commonly occurs to form relief microscale structures (such as holes or drops) on a substrate if the thickness is incommensurate with an intrinsic spacing of ordered nanodomains.[1−6] Upon annealing at high temperature or exposure to solvents, the film surface acquires an undulating thickness so that the film stature becomes quantized in integer (symmetric wetting) or 1.5 integer (asymmetric wetting) units of the nanodomain spacing, depending on the preferential wetting with air or the substrate interface by each block. Such a feature is typical for symmetric BCP.[1−6] For an asymmetric BCP, the morphology of a thin film is more complicated than for a symmetric BCP. Not only variations in spatial orientation of nanostructures but also surface-induced phase transitions evolve during dewetting.[7−9]

Grazing-incidence small-angle X-ray scattering (GISAXS) is a powerful tool to probe a surface or interface and buried nanostructures in thin films, such as islands on a substrate or buried nanoparticles within a film.[10−12] Beyond the structural information in and out of the plane of a thin film given by GISAXS, this experiment provides also insight into the morphology of a nanofaceted surface of crystals randomly registered on a substrate.[12] The GISAXS patterns of systems with nanofaceted surfaces typically reveal diffuse scattering streaks at angles with respect to the normal to the substrate surface; this phenomenon is summarized in a comprehensive review.[12] These diffuse scattering streaks of GISAXS have been reported for only semiconductor quantum dots or metal nanoparticles grown on a substrate.[12] Little is understood about the GISAXS patterns of relief terraces with a facet-like wedge in a destabilized BCP thin film. Here we report diffuse scattering streaks of GISAXS for dewetted morphologies in P(S-*b*-MMA) thin films consisting of ordered mesophase-separated nanodomains on a bare silicon substrate and substrates coated with end-grafted PMMA and PS brushes, respectively denoted SiO_x/Si, PMMA−SiO_x/Si and PS−SiO_x/Si for brevity. By analyzing the diffuse streaks we aimed to acquire an understanding of the hierarchical ordering of P(S-*b*-MMA) nanostructures on thermal annealing. This system thus serves as a model to analyze terraces induced by dewetting and with facet-like surfaces in a destabilized BCP thin film by GISAXS.

*Author to whom correspondence should be addressed: E-mail: yssun@cc.ncu.edu.tw.

Experiments

Preparation and Characterization of Materials. Hydroxyl-terminated polystyrene (PS−OH, M_n = 6 kg/mol, index of polydispersity I_p = 1.07), hydroxyl-terminated poly(methyl methacrylate) (PMMA−OH, M_n = 6 kg/mol, I_p = 1.06), and polystyrene- *block*-poly(methyl methacrylate) (P(S-*b*-MMA), M_n = 82 kg/mol, f_{ps} = 72% and f_{PMMA} = 28%, I_p = 1.07) were used as received (from Polymer Source, Inc.). The surface of the substrate end-grafted with PMMA and PS sublayers was modified according to the reported protocol.[13] P(S-*b*-MMA) thin films of initial film thickness 38.4 nm were prepared on SiO_x/Si, PS−SiO_x/Si and PMMA−SiO_x/Si substrates via spin coating (5000 rpm, 30 s) from a solution (1.6 mass %) in toluene. Annealing at 210 °C was implemented in a closed hot stage (HCS402 Instec) purged with N_2. To observe the nanodomains, and dewetted morphologies, we characterized the surface of the thin films with an atomic-force microscope (AFM, SPA400 Seiko) in the tapping mode. For the AFM measurements, we used aluminum-coated silicon cantilevers (length 125 μm, width 30 μm and thickness 4 μm). The force coefficient is approximately 42 N/m; the resonant frequency is 330 kHz. Small-angle X-ray scattering (GISAXS) in a grazing-incidence geometry at five angles—0.1, 0.15, 0.1875, 0.21, and 0.25°—was performed to characterize nanostructures of the annealed P(S-*b*-MMA) films with an X-ray beam of photon energy 8 keV (wavelength, λ = 1.55 Å) at beamline BL23A, National Synchrotron Radiation Research Center (NSRRC), Hsinchu. The configuration of the GISAXS at BL23A was detailed elsewhere.[14] The critical angles of P(S-*b*-MMA) and silicon substrates measured with X-ray reflectivity (XR) are 0.1860 ($\alpha_c^{P(S\text{-}b\text{-}MMA)}$) and 0.2294° ($\alpha_c^{Si}$), respectively.[15] The range of grazing- incidence angle (α_i) thus covered fully the critical angles of both the P(S-*b*-MMA) film and the substrate. The distance from the sample to the detector was 1926.7 mm. The scattering vector, q ($q = 4\pi/\lambda(\sin\theta)$, with scattering angle θ), in these patterns was calibrated with silver behenate. The films were mounted on a z-axis

 Published on Web 08/02/2010

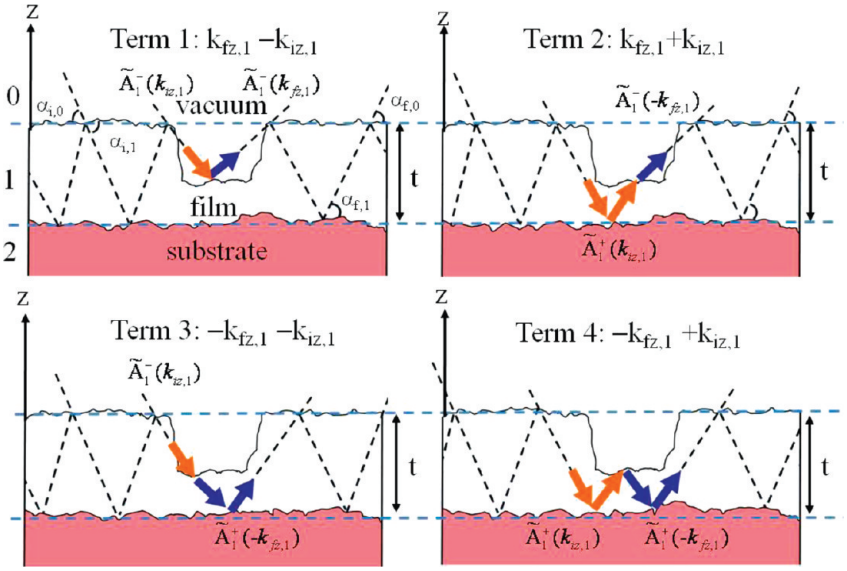

Figure 1. Schematic diagram of the four terms involved in the scattering by a hole in a layer covering over a substrate.

goniometer. 2D GISAXS patterns were typically collected with a MAR CCD detector for 180−300 s.

Theory of GISAXS

In contrast to modeling of SAXS data mainly expressed in terms of the Born approximation (BA), GISAXS data reveal complicated scattering patterns or profiles as a result of multiple scattering events in terms of a combination of reflection and refraction effects.[11,12] Recently, as shown in the comprehensive review by Renaud et al., GISAXS modeling analyses can be well achieved using the distorted-wave Born approximation (DWBA), in which the total DWBA amplitude can be expressed as a coherent sum of four scattered amplitudes.[12] Each of the four scattered amplitudes originates from a different scattering path. As a result, the scattering cross section can be expressed as[11,12]

$$\frac{d\sigma}{d\Omega} = \frac{{k_0}^4}{16\pi^2}|\Delta n|^2|\mathcal{R}(q_{||}, k_{iz,0}, k_{fz,0})|^2 \quad (1)$$

where Δn is the contrast of dielectric constant, and $q_{||}$ is the component of the wavevector transfer ($q = k_f - k_i$, in which k_i and k_f represent the wavevector of the incident and scattered X-rays) parallel to the surface.

In this study, only the GISAXS formulas of the specific morphology, namely holes in a layer covering over a substrate, are quoted here for either qualitatively interpreting or quantitatively modeling GISAXS data. For relief structures between irregular holes as a result of film instability, their four scattered events are schematically illustrated in Figure 1 and the corresponding GISAXS formulas are given as follows.

In the geometry of holes in a layer covering on top of a substrate, the contrast of dielectric constant is given as[11,12]

$$\Delta n^2 = {n_{hole}}^2 - {n_{layer}}^2 = 1(vacuum) - {n_{layer}}^2 \quad (2)$$

where n_{layer} is the dielectric constant of an overlayer.

The total scattering amplitude of holes in a layer on a substrate is expressed by

$$\begin{aligned}&\mathcal{R}(\mathbf{q}_{||}, k_{iz,0}, k_{fz,0})\\ &= \tilde{A}_1^-(k_{iz,1})\tilde{A}_1^-(-k_{fz,1})F(\mathbf{q}_{||}, +k_{fz,1} - k_{iz,1})\\ &\quad + \tilde{A}_1^+(k_{iz,1})\tilde{A}_1^-(-k_{fz,1})F(\mathbf{q}_{||}, +k_{fz,1} + k_{iz,1})\\ &\quad + \tilde{A}_1^-(k_{iz,1})\tilde{A}_1^+(-k_{fz,1})F(\mathbf{q}_{||}, -k_{fz,1} - k_{iz,1})\\ &\quad + \tilde{A}_1^+(k_{iz,1})\tilde{A}_1^+(-k_{fz,1})F(\mathbf{q}_{||}, -k_{fz,1} + k_{iz,1}) \quad (3)\end{aligned}$$

with

$$\frac{A_1^-}{A_0^-} = \tilde{A}_1 - = \frac{T_{0,1}}{1 + R_{0,1}R_{1,2}e^{2ik_{z,1}t}} \quad (4)$$

and

$$\frac{A_1^+}{A_0^-} = \tilde{A}_1 + = \frac{T_{0,1}R_{1,2}e^{2ik_{z,1}t}}{1 + R_{0,1}R_{1,2}e^{2ik_{z,1}t}} \quad (5)$$

where $R_{0,1}$ and $R_{1,2}$ represent the reflectivity coefficient at the vacuum-layer and layer-substrate interfaces respectively whereas $T_{0,1}$ denotes the transmittance coefficient at the vacuum-layer interface, and t represents the thickness of a film. Consequently, the reflectivity of the layer can modulate the scattering amplitudes of relief structures by giving various weighting coefficients, which are sensitive to grazing incident angle α_i.[11]

The amplitudes F depend on ($q_{||}$, $\pm k_{fz,j} \pm k_{iz,j}$), and can be given in terms of the Fourier transform of the particle shape[11,12]

$$F(q) = \int p(r)e^{iq\cdot r}\,dr \quad (6)$$

where $p(r)$ is the shape function of an object. In eq 6, integrating over the volume $V(r)$ in the particle form factor gives

$$F(q) = \int_{V(r)} e^{iq\cdot r}\,d^3r \quad (7)$$

As shown in the early work by von Laue,[16] the volume integral can be transformed into a surface integral by applying the Green's divergence theorem, which yields[12,16]

$$F(q) = -\frac{1}{q^2}\int_{s(r)}\frac{\partial e^{iq\cdot r}}{\partial n}\,d^2r = -\frac{1}{q^2}\int_{s(r)} q_n e^{iq\cdot r}\,d^2r \quad (8)$$

where q_n is the component of q along an outward normal direction n of a surface.

In the case of a flat surface p with constant q_n, eqn-8 can be further simplified as

$$F(q) = -\frac{iq_n}{q^2}e^{iq\cdot r_n}\int_p e^{iq\cdot r'}\,d^2r' \quad (9)$$

As a result, eqn-9 indicates that the maximum of the intensity distribution is along the normal direction of the surface, for which

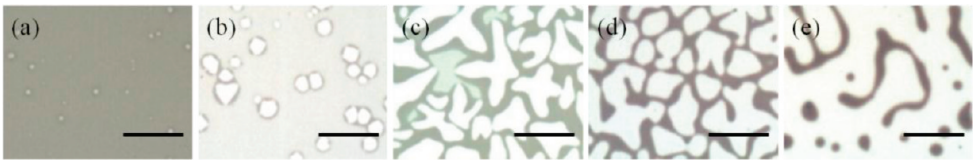

Figure 2. Reflection optical micrographs of P(S-*b*-MMA) films (thickness 36.4 nm) after isothermal annealing for 12 h at temperatures (a) 170, (b) 190, (c) 210, (d) 230, and (e) 245 °C. The varied color in the OM images indicates the variations in film thickness. The scale bar is 20 μm.

the amplitude decays as q^{-1}. Therefore, the intensity expressed in terms of the square of the amplitude gives the dependence of the intensity on q^{-2}.[16−18]

Results and Discussion

Dewetting Morphologies in Thin Films. The reflective optical micrographs in Figure 2 show the dewetted morphologies of isothermally annealed films. Upon annealing at temperatures 170, 190, 210, 230, and 245 °C for 12 h, the P(S-*b*-MMA) films dewetted on SiO_x/Si via a mechanism of nucleation and growth, causing the film surface to acquire an undulating thickness. The morphological evolution of dewetting occurred in four stages − rupture of the film (Figure 2a), formation of holes with uneven wavy rims (Figure 2b), progressive growth of the rims until impinging together to form a polygonal network (Figure 2, parts c and d), and final breaking of the polygonal network into drops or strings (Figure 2e).

Relief Structures between Irregular Holes. As the AFM images in Figure 3 show, the P(S-*b*-MMA) films of initial thickness 38.4 nm, which is incommensurate with a stable size for asymmetric wetting, severely dewetted on SiO_x/Si and PMMA−SiO_x/Si to form relief terraces upon annealing (Figure 3, parts a and b) whereas the P(S-*b*-MMA) film of the same thickness, being commensurate for symmetric wetting, remained stable on PS−SiO_x/Si (Figure 3c). Because of the preferential wetting of the free surface by the PS block, the feature of nanodomains is clearly observable only at the edge of terraces on SiO_x/Si and PMMA−SiO_x/Si, as shown in the 2 μm × 2 μm AFM height and the phase images. The corresponding 3D AFM topography reveals the height of the relief microstructures to be about 38 nm (Figure 3, parts d and e); this thickness is appropriate for a single layer of the P(S-*b*-MMA) film that comprises one row of parallel PMMA cylinders embedded within a PS matrix (shown in the bottom AFM phase images of Figure 3, parts a and b). The X-ray reflectivity data indicate that the underlying layer is a monolayer (thickness 21 nm) of autophobic P(S-*b*-MMA) brushes with the PMMA blocks facing SiO_x/Si or PMMA−SiO_x/Si but the PS blocks outward to air.[15] As a result, the destabilized P(S-*b*-MMA) films are seen to have a top layer of unanchored P(S-*b*-MMA) partially wetting with a self-similar species (namely, a monolayer of anchored P(S-*b*-MMA) brushes) at contact angles in the range 4−6.5° on SiO_x/Si and PMMA−SiO_x/Si (Figures 3, parts d and e).

To characterize the buried mesophase-separated nanostructures of the P(S-*b*-MMA) films on SiO_x/Si, PMMA−SiO_x/Si and PS−SiO_x/Si substrates after isothermal annealing, we measured GISAXS at five incident angles (0.1, 0.15, 0.1875, 0.21, and 0.25°). As Figure 4 shows, the 2D GISAXS diffraction patterns for the destabilized films exhibit rod-like or spot-like scattering typical of strongly fiber-textured films regardless of incident angles, indicating that the nanodomains of the dewetted/wetted P(S-*b*-MMA) films on SiO_x/Si, PMMA−SiO_x/Si and PS−SiO_x/Si were highly oriented in the plane of the substrate. Furthermore, the two streaks parallel to the $q_{\|}$ direction typically resulting from standing waves interfere coherently with the Bragg rods, producing diffraction spots.[19] As these spots are due to the effect of standing waves, the diffraction intensity of the spots varied with the incident angle. Another cause of variations of intensity and of the $q_\perp$ position of the Bragg spots with grazing angle is a complicated effect of both reflection and refraction of an X-ray beam within a film.[8,11,12] At small grazing angles less than α_c^{Si} ($\alpha_i < \alpha_c^{Si}$), an additional set of $q_\perp$-component diffraction spots is present for the destabilized P(S-*b*-MMA) on SiO_x/Si and PMMA−SiO_x/Si but absent from the film on PS−SiO_x/Si. At angles near α_c^{Si} or above ($\alpha_i \geq \alpha_c^{Si}$), the GISAXS patterns for the P(S-*b*-MMA) films on the substrates of three kinds almost exhibit a similar feature of the $q_\perp$-component diffraction spots, indicative of the same orientation and mesophase-separated nanodomains.

When the detector-scan profiles with intensity as a function of $q_\perp$ were obtained with a vertical slice at $q_{\|} = 0$, typical Kiessig fringes are clearly observed in the one-dimensional (1D) scattering curves. As shown in Figure 5, parts a and b, the 1D GISAXS profiles for the destabilized films on SiO_x/Si and PMMA−SiO_x/Si reveal fringes along the vertical direction at $q_{\|} = 0$. In contrast, the P(S-*b*-MMA) film on PS−SiO_x/Si shows no feature of fringes, as shown in Figure 5c. Those fringes are associated with resonant diffuse scattering as a result of correlated interfaces.[15,20,21] Namely, the free interface of thin films on SiO_x/Si and PMMA−SiO_x/Si have a partially identical roughness contour with the surface roughness of a substrate.[15,20,21] On the basis of the frequency of the fringes observed for thin films on SiO_x/Si and PMMA−SiO_x/Si, the correlated thickness d^{cor} was estimated as 20−21 nm via $\Delta q_\perp = 2\pi/d^{cor}$, indicating that the fringes originate from the anchored P(S-*b*-MMA) monolayer rather than the entire film. Besides, we noted variations in the $q_\perp$ position of fringes with varied α_i. This phenomenon can be explained by the interplay between the multiple scattering events, as illustrated in Figure 1. As shown in the early modeling of GISAXS data by Lazzari et al. with the DWBA approximation, the interference between the scattering events, in which the contributions of their amplitude and phase to an overall intensity profile varied with α_i, modulated the position and the intensity of fringes.[11]

As Figure 6 shows, the corresponding in-plane 1D GISAXS result for the destabilized P(S-*b*-MMA) films measured at 30 °C features sharp diffraction peaks located at $q_{\|} = 0.0143$, 0.0280, and 0.0414 Å^{-1} (indicated by arrows). These features with $q_{\|}$ ratios $1:4^{1/2}:9^{1/2}$ are clearly discerned. However, the peak at $q_{\|} = 0.0246$ Å^{-1} that corresponds to the $q_{\|}$ ratio of $3^{1/2}$ with respect to the position of the principal Bragg peak is absent. This $3^{1/2}$ peak typically associated with the diffraction of the {11} plane only can be observable for ordered structures with a hexagonal lattice.[10] Thus, the absence of the $3^{1/2}$ peak can be taken as an indication of the PMMA nanodomains lacking a hexagonal order within a PS matrix. Because of an affinity between the PMMA block and the polar substrate, the PMMA nanodomains are preferably oriented parallel to the substrate surface. Since a

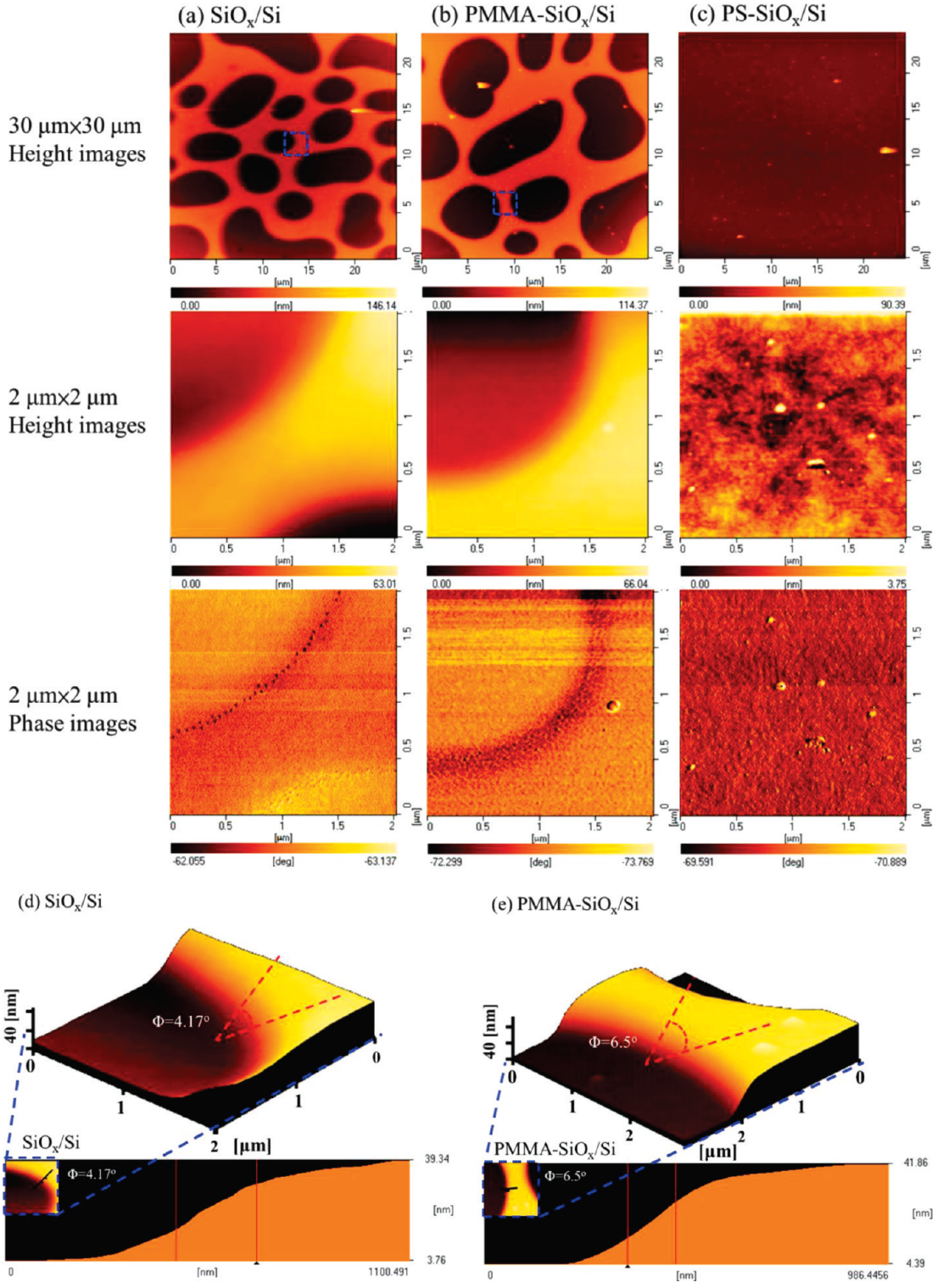

Figure 3. The 30 μm × 30 μm (top row) and 2 μm × 2 μm (middle row) AFM height images and 2 μm × 2 μm (bottom row) phase images for P(S-*b*-MMA) films of initial thickness 38.4 nm spread on substrates of three kinds: (a) SiO_x/Si, (b) PMMA−SiO_x/Si, (c) PS−SiO_x/Si, after isothermal annealing at 210 °C for 12 h. The corresponding 3D topographical images and line scans for P(S-*b*-MMA) on SiO_x/Si (d) and PMMA−SiO_x/Si (e) are also shown for comparison. The dotted squares represent the magnified areas of the images of 30 μm × 30 μm, as a visual guide.

monolayer thickness of P(S-*b*-MMA) films was spin-coated on the substrates, only one row of PMMA cylinders with a parallel orientation contributed the $q_{\|}$ Bragg peaks in a series with a long period.

Furthermore, the degree of ordering in the destabilized P(S-*b*-MMA) films is greater than that in the intact P(S-*b*-MMA) film on PS−SiO_x/Si. This deduction is supported by evidence that the width of the principal Bragg peak ($q_{\|}$*) for films on SiO_x/Si (the full width at half-maximum, $\Delta q_{\|}$*, ranges from 1.94×10^{-3} to 2.11×10^{-3} Å^{-1}) and PMMA−SiO_x/Si (in the range 1.77×10^{-3} to 2.0×10^{-3} Å^{-1}) is less than that for the film on PS−SiO_x/Si (in the range 2.26×10^{-3} to 2.97×10^{-3} Å^{-1}). In contrast, the position of the principal feature shown in the GISAXS profiles of the

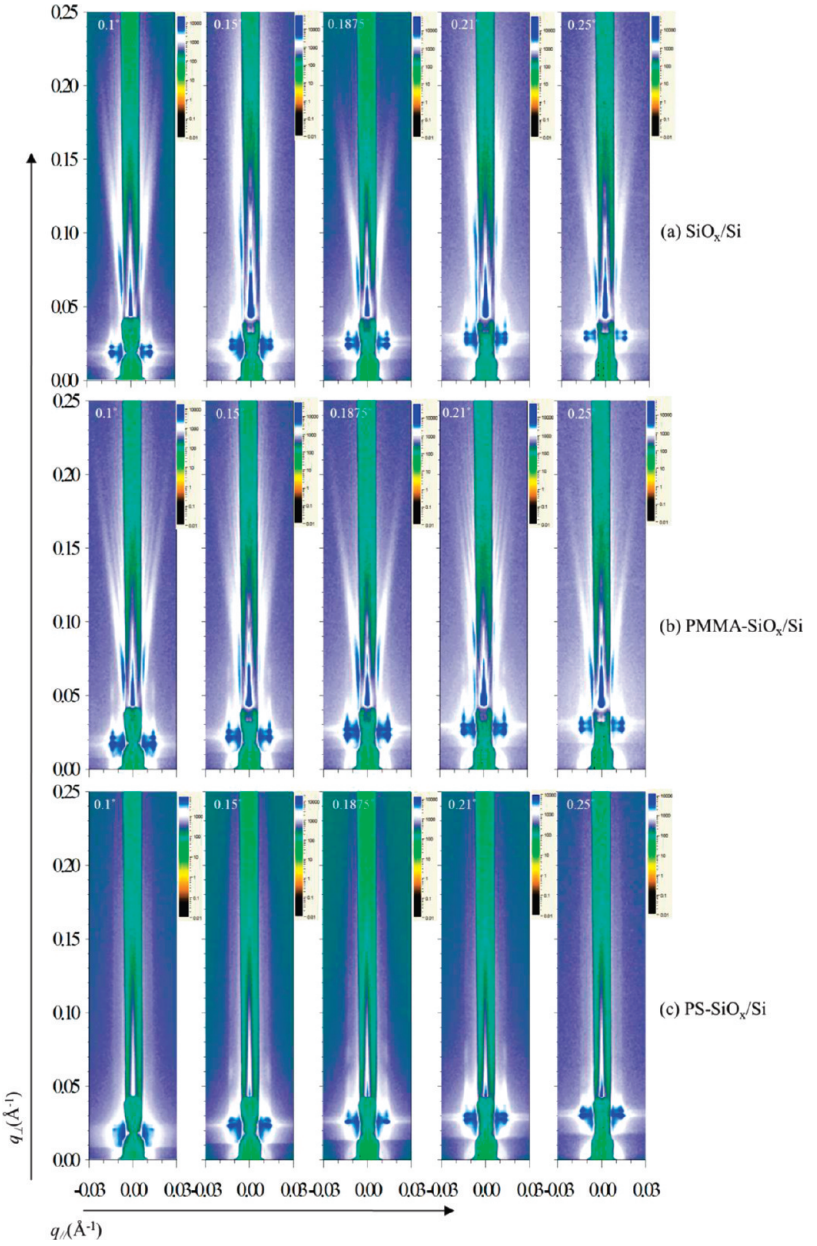

Figure 4. 2D patterns of GISAXS measured at various angles (α_i = 0.1, 0.15, 0.1875, 0.21, and 0.25°) of grazing incidence for P(S-*b*-MMA) thin films of initial thickness 38.4 nm, spread on substrates of three kinds: (a) SiO_x/Si, (b) PMMA−SiO_x/Si, (c) PS−SiO_x/Si, after isothermal annealing at 210 °C for 12 h.

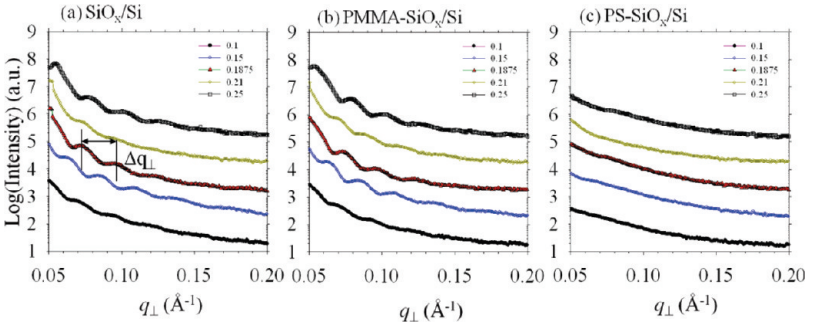

Figure 5. 1D detector-scan profiles as a function of $q_\perp$ obtained with vertical cuts at $q_{||} = 0$ Å^{-1} corresponding to Figure 4 (substrates: (a) SiO_x/Si, (b) PMMA−SiO_x/Si, and (c) PS−SiO_x/Si). The curves were shifted for clarity along the *y* axis.

destabilized P(S-*b*-MMA) films remains unaltered with varied α_i, whereas the position of the principal feature varied with α_i for the film on PS−SiO_x/Si. This result implies that the destabilized P(S-*b*-MMA) films achieve a film thickness commensurate with a natural spacing of PMMA nanodomains by surface undulations of the film thickness, improving the

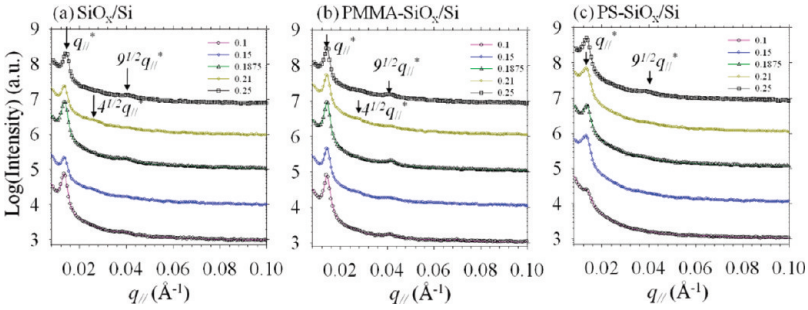

Figure 6. 1D in-plane profiles as a function of $q_{\|}$ obtained with horizontal cuts at $q_{\perp} = 0.022$ Å^{-1} corresponding to Figure 4. (substrates: (a) SiO_x/Si, (b) PMMA−SiO_x/Si, and (c) PS−SiO_x/Si). The curves were shifted for clarity along the y axis, and the Bragg peaks were labeled by arrows.

order. For the P(S-*b*-MMA) film on PS−SiO_x/Si, the thickness 38.4 nm of a film as spun initially coincides with a natural spacing of nanodomains, so that the energy of initiating dewetting is too great to form relief microstructures. Instead, small grains with a large density of defects are produced as a result of unfavorable stretching of the chains.[15,22−27] The shift of the principal Bragg feature to small values of the $q_{\|}$ position with varied α_i is thus accompanied by the broadening of the diffraction feature. Such a feature was also reported in the morphological study of triblock copolymer thin films on various types of substrates by using grazing incident small-angle neutron scattering (GISANS).[27] They attributed the feature to variances in ordering of nanodomains at surface and buried in bulk. On the basis of the feature appearing in the Figure 6, we proposed a scenario to interpret the discrepancy in the ordering of nanostructures for thin films on polar (SiO_x/Si and PMMA−SiO_x/Si) and nonpolar substrates (PS−SiO_x/Si). On a polar substrate, P(S-*b*-MMA) thin films have asymmetric wetting boundaries since the PS block with a lower surface energy prefers wetting with the air interface while the preference wetting with the substrate interface (SiO_x/Si and PMMA−SiO_x/Si) is dominated by the PMMA block. Therefore, the initial film thickness of 38.4 nm for thin films on SiO_x/Si and PMMA−SiO_x/Si is incommensurable with a stable length in terms of nD+β for asymmetric wetting boundaries (D represents the interdomain spacing, n is an integral and β the thickness of a wetting layer).[22−26] Therefore, the films on the polar substrate are highly metastable. Upon heating, the undulation of the film thickness produces relief structures with their height becoming satisfied with commensurability.[15] By contrast, the thin film on a nonpolar substrate has symmetry wetting boundaries since the PS block prefers wetting the both interfaces. Thus, the initial thickness of the thin film on PS−SiO_x/Si is very comparable to the length for a stable film (i.e., nD for symmetric wetting boundaries). Therefore, a large-scale undulation in film thickness is highly prohibited, but instead only small-scale stretching of polymer chains is allowable so as to satisfy the commensurability condition. However, the chain stretching further gave rise to a perturbation in the domain spacing, and also led to surface roughening at the free interface.[15] On the other hand, for the thin film lacking large-scale undulations of the film thickness on PS−SiO_x/Si, the structure organization to improve domain ordering would take a longer time scale during thermal annealing. Therefore, after annealing at 210 °C for the same period of time the thin film on PS−SiO_x/Si had a low degree of domain ordering in comparison with that on SiO_x/Si and PMMA−SiO_x/Si.

Another intriguing observation is that narrow but diffuse scattering streaks are present at ca. 6° ($\xi = 6°$) with respect to the $q_{\perp}$ direction for the destabilized P(S-*b*-MMA) thin films on SiO_x/Si and PMMA−SiO_x/Si (*cf.* Figure 4). In contrast, these diffuse scattering streaks are absent from GISAXS patterns of the P(S-*b*-MMA) film fully wetting on PS−SiO_x/Si. These streaks might be attributed to diffuse scattering from the edge of terraces. The GISAXS pattern recorded at $\alpha_i = 0.1°$ shows a splitting of the diffuse scattering streaks. The intensity of the double or multiple streaks depends strongly on the angles of grazing incidence for the GISAXS collection. At grazing angle $\alpha_i = 0.25°$, only the lower set of diffuse scattering streaks remained, indicating that the upper set of diffuse scattering streaks originates from reflected X-ray beams whereas the lower set of diffuse scattering streaks originates from refracted X-ray beams. The reason is that the scattering intensity, in particular $\alpha_i \gg \alpha_c$, from the reflected beam decreases abruptly.[8] These phenomena are explained satisfactorily in terms of DWBA of GISAXS.[11,12]

According to the AFM topographies shown in Figure 3, we proposed that the destabilized P(S-*b*-MMA) films having a polydispersive population of relief structures between irregular holes contribute the diffuse scattering streaks observed in the 2D GISAXS patterns. In order to analyze the peak width of the diffuse streaks, we have extracted line scans by an off-detector-scan cut through the diffuse streaks.

Figure 7 shows the 1D off-detector-scan scattering profiles, which were extracted from the vertical scan cuts of the principal feature at $q_{\|} = 0.0142$ Å^{-1}, as shown in the 2D GISAXS patterns, along the $q_{\perp}$ direction. In addition to the out-of-plane scattering profiles consisting mainly of oscillations previously explained in terms of the effects of standing waves and combined reflection and refraction, a broad hump at $q_{\|}$ above 0.1 Å^{-1} is clearly observable for the destabilized P(S-*b*-MMA) films (Figures 7, parts a and b). In contrast, this hump is absent from the profiles of the intact P(S-*b*-MMA) film on PS−SiO_x/Si (Figure 7c). It has been shown that the full width at half-maximum (fwhm) of streaks is inversely proportional to the average facet size.[17,18] However, the fwhm of the streak in the destabilized P(S-*b*-MMA) films seems too large. As the relief terraces occur on a micrometer scale, the fwhm of the diffuse scattering streak for an individual terrace should appear much smaller.[18] The broad fwhm of the hump seems to be due to a sum of diffuse scattering from the ensemble of individual terraces with contact angles in the range 4−6°, as observed from the AFM images.

On the other hand, for samples having a large-polydispersity of relief structures, the asymptotic behavior of the mean form factor can be described by the Porod approach.[28] That is, the intensity of the form factor decays as q^{-n}. Revenant et al., demonstrated that for a particle shape having sufficiently large size distribution, $n_{\|} = 2.5$ (along the intensity as a function of $q_{\|}$) or $n_{\perp} = 3$ (along the intensity as a function of $q_{\perp}$) were obtained for a cylinder whereas $n_{\|} = 3$ or $n_{\perp} = 4$

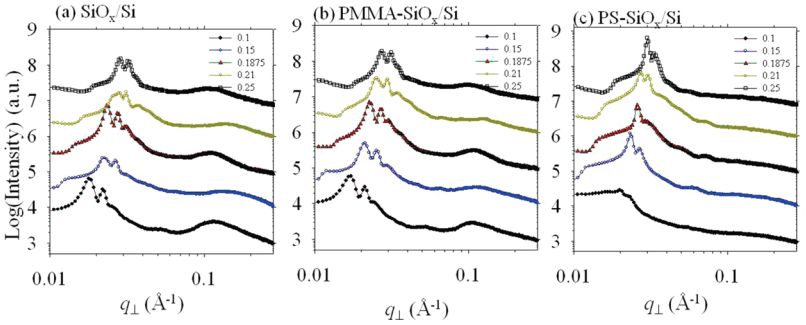

Figure 7. 1D out-of-plane profiles as a function of $q_\perp$ obtained with vertical cuts at $q_\parallel = 0.0142$ Å^{-1} corresponding to Figure 4 (substrates: (a) SiO$_x$/Si, (b) PMMA−SiO$_x$/Si, and (c) PS−SiO$_x$/Si). The curves were shifted for clarity along the y axis.

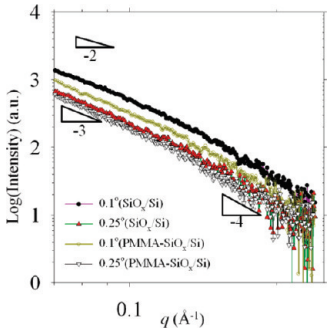

Figure 8. 1D profiles extracted along the diffuse scattering streaks at angle 6° with respect to the $q_\perp$ direction from 2D GISAXS patterns collected at $\alpha_i = 0.1$ and 0.25° shown in Figure 4. The three triangles, each of which has a slope of −2 or −3 or −4, are plotted as a visual guide.

in an accessible q range were found for a hemisphere or pyramid.[28] Thus, one-dimensional 1D profiles with intensity as a function of q obtained by a scan cut along the streaks are shown to reveal the asymptotic power law behavior form. To precisely determine the asymptotic behavior, a background was obtained by a scan cut with an offset of $\Delta\xi = 2°$ with respect to the diffuse streaks and its intensity was subtracted from the corresponding 1D profile of the diffuse streaks. Along the streaks the intensity at the small q region decreases as a function of q with exponent −3, as shown in Figure 8. For comparison, at the large q region, the intensity decays as q^{-4}, indicative of a Porod law for surface scattering from smooth-surfaced objects with a sharp interface.[29] For monodispersive faceted crystals with a sharp surface, the intensity of streaks decays as q^{-2} whereas for either nonfaceted crystals with a rounded surface or straight edges of intersections of facets the intensity decays as q^{-4}.[17,18] In the case of relief dewetted P(S-*b*-MMA) microstructures, the q^{-3} dependence of the intensity decay indicates that the relief terraces are a structure intermediate between regularly faceted ordered microstructures and nonfaceted crystallites with a rounded surface. Scrutiny of the 3D AFM images, as shown in Figure 3, parts d and e, indicates that the areas at which the smooth surfaces at the top and base of the terraces join exhibit a rounded shape, confirming the argument proposed based on the GISAXS evidence. The curved shape at the base (the contact line) is due to partial wetting of the P(S-*b*-MMA) top layer on a monolayer of autophobic P(S-*b*-MMA) brushes anchored onto SiO$_x$/Si or PMMA−SiO$_x$/Si. Between the top and base corners with a curved surface the relief terraces display a wedge-shaped edge; such an edge appears analogous to the nanofacetting of a crystalline-faceted object.[17,18] The q^{-3} dependence of the intensity along the diffuse scattering streaks is therefore due to a superimposed scattering from the polydispersive relief terraces with rounded surfaces on the top and base and with a facet-like wedge on the edge. Unlike the fringes having an oscillating period along the vertical direction at $q_\parallel = 0$, such a feature damps out along the diffuse streaks. The cause of this damping of fringes along the diffuse streaks is that each large relief terrace has varied size and angle between the wedge and the base of the terraces. The sum of diffuse scattering that originates from the ensemble of facet-like wedges with varied size and contact angle thus smears out these fringes.

Modeling of GISAXS Data. In order to clearly understand morphological characteristics of relief structures between irregular holes, we implemented GISAXS modeling analyses. Figure 9 is schematic illustrations showing the real space and of corresponding reciprocal space of cylindrical nanodomains oriented to the film surface for a destabilized thin film on top of either SiO$_x$/Si or PMMA−SiO$_x$/Si. The real space displays that on the polar substrate the top layer of the destabilized P(S-*b*-MMA) film comprises one row of PMMA nanocylinders with a parallel orientation embedded within a PS matrix. Film instability causes a hole within the top layer of unanchored P(S-*b*-MMA) of 38 nm. The hole has a depth H of 38 nm with a depth deviation σ_H in the range of 0.01 to 0.3 and base radius R of 1000 nm with a radius deviation σ_R in the range of 0.01 to 0.3. Under the layer is a 21 nm wetting monolayer of P(S-*b*-MMA) with the PMMA blocks end-anchoring on a substrate.

The real-space diagrammatic representation of Figure 9 is analogous to that of a hole in a layer on top of a substrate as a model of simulating the GISAXS data. The cone shape for describing a hole was used in the modeling of GISAXS data since the irregular holes, as displayed in the AFM topographies of Figure 3, are analogous to the cone shape. The analytic expressions of the form factor of the cone shape have been given in refs 11 and12. We assume that the positions of relief structures between holes are completely random and independent without a positional correlation. In addition, the relief structures between holes are isotropic in the $X-Y$ plane, and the axis of holes is normal to the substrate surface. Since identification of the shape of relief structures by analyzing diffuse scattering streaks is the subject of the study (*cf.* the reciprocal space of Figure 9), thus simulating the scattering spots/rods associated with mesophase-separated cylindrical nanostructures embedded within the relief structure was not considered in the modeling of GISAXS patterns for simplification. As a result, the simulated diffuse GISAXS scattering streaks are mainly contributed from the form factor of relief structures on a micrometer length scale.

Figure 10 shows 2D maps of $|F(q)|^2$ in the $(q_\parallel, q_\perp)$ space simulated within the DWBA for various grazing incidence angles α_i. A comparison of the experimental (Figure 4) and simulated GISAXS patterns (Figure 10) reveals that the

diffuse streaks at angles with respect to $q_\perp$ can be well reproduced assuming the cone shape with a base angle ξ of 6° for simulating irregular holes. As shown in Figure 10, the simulated GISAXS maps reveal scattering streaks, corresponding to the facet-like wedge with the base angle 6° at the edge of relief structures. For α_i = 0.1°, the reflected beam contributed the streaks whereas for α_i = 0.25° the transmitted beam contributed the streaks. In the GISAXS maps calculated for α_i = 0.21°, the streaks were found to be double due to an effect of superposition of the refraction and reflection beams (indicated by the arrows). The upper streak is due to the reflected beam whereas the lower one is ascribed to the transmitted beam.

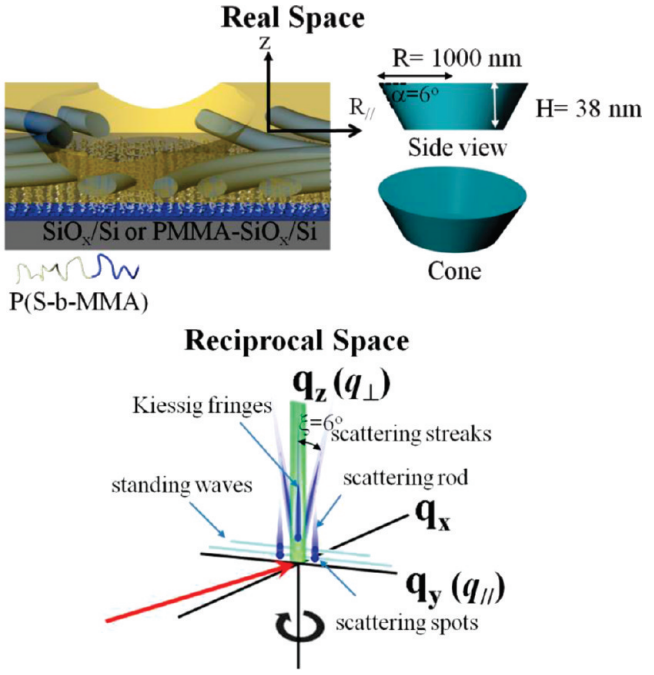

Figure 9. Schematic illustrations showing the real space and reciprocal space of parallel PMMA cylinders within the top layer of unanchored P(S-*b*-MMA) that is capped on a wetting monolayer of anchored P(S-*b*-MMA). Film instability causes a hole in the top layer presenting in the real space. The based angle α = 6° is denoted as the contact angle modeling for a facet-like wedge at the edge of relief structures. The cone represents as a hole, within a film of 59 nm on a substrate. The scattering features, such as rod-like/spot-like scattering, diffuse scattering streaks, and Kiessig fringes, were schematically illustrated in the reciprocal space.

To gain a better understanding of the relief structures, we implemented the detector−scan (at $q_{||}$ = 0 Å^{-1}) and off−detector−scan (at $q_{||}$ = 0.0143 Å^{-1}) cuts on the 2D simulated GISAXS patterns to show the 1D scattering profiles.

As shown in Figure 11a, the simulated 1D detector−scan profiles reveal the dependence of fringes on α_i, in which the two oscillating frequencies, due to the depth thickness of a cone (high-frequency $\Delta q_\perp{}^1$) and to the underlying monolayer thickness (low-frequency $\Delta q_\perp{}^2$), are observable. The cone thickness is dominating the fringes with $\Delta q_\perp{}^1$ as $\alpha_i < \alpha_c{}^{P(S\text{-}b\text{-}MMA)}$ or $\alpha_i > \alpha_c{}^{Si}$ whereas a monolayer thickness is dominating the fringes with $\Delta q_\perp{}^2$ in the region $\alpha_c{}^{P(S\text{-}b\text{-}MMA)} < \alpha_i < \alpha_c{}^{Si}$. The presence of the fringes with $\Delta q_\perp{}^1$ in Figure 11a is absent from those experimentally measured at various α_i shown in Figure 5, in which only reveals fringes associated with the 21 nm wetting monolayer of anchored P(S-*b*-MMA). None of the fringes shown in Figure 5 is due to the entire thickness of a film or the depth thickness of a hole. Causing the discrepancy is explained as follows. First, the reflection and transmission coefficients in the simulated GISAXS patterns are simulated based on the assumption of an uncorrelated roughness at interfaces (*cf.* eqs 3 and 4). For uncorrelated roughness layers, all the interfaces scatter independently, and the intensity of the diffuse scattering is therefore an incoherent sum of scatters from individual interfaces. Thus, the intensity of fringes is only enhanced once the incident and scattered angle satisfies the Bragg law, giving rise to fringes with an oscillating period ($\Delta q_\perp$) being related to the thickness d^{uncor} of a film having uncorrelated interfaces via $\Delta q_\perp = 2\pi/d^{uncor}$. In the case of uncorrelated rough interfaces, the amplitude of fringes mainly relies on whether the film interfaces have identical mean roughness thicknesses (i.e., root-mean-square surface roughness).[30] For the simulated GISAXS patterns/profiles, the interfaces

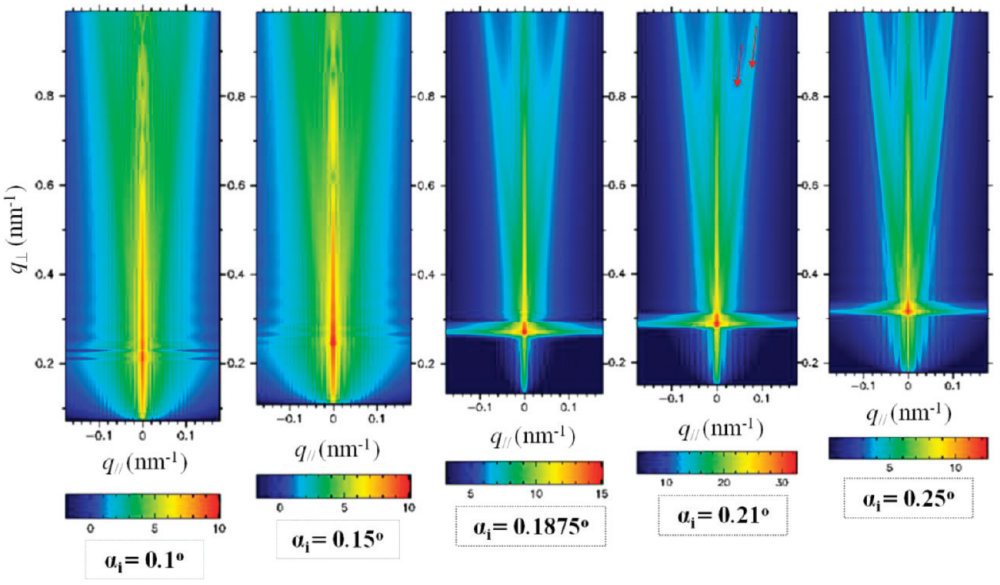

Figure 10. Simulated 2D GISAXS patterns based on the shape of a cone with a base angle of 6°, thickness of 38 nm and radius of 1000 nm. The base radius of the cone has a Gaussian size distribution with the radius deviation σ_R of 0.01 while the thickness of the cone has a Gaussian size distribution with the high deviation σ_H of 0.2. The intensity is represented with a logarithmic scale. The grazing incident angles used in the simulation are indicated.

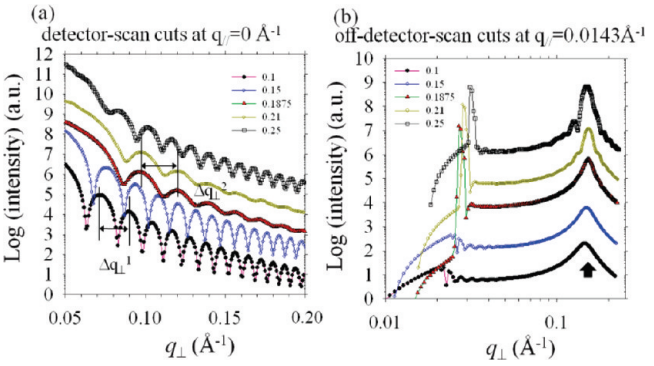

Figure 11. (a) 1D detector-scan profiles and (b) off-detector-scan profiles as a function of $q_\perp$ obtained with vertical cuts at $q_\parallel = 0$ Å^{-1} and $q_\parallel = 0.0143$ Å^{-1} respectively, corresponding to Figure 10. The curves were shifted for clarity along the y axis.

are assumed to be uncorrelated and to have identical mean roughness thicknesses. Thus, the interference between the scattering due to the hole depth (i.e., the cone thickness) and that associated with the entire film leads to the fringes with the two periods of oscillation, in which the position and amplitude of intensity maxima strongly depend on α_i. By contrast, for correlated rough layers, complete or partial roughness replication at interfaces gives rise to resonant diffuse scattering with its intensity being coherently concentrated in narrow sheets.[20,21,31] As a result, surface roughness correlation at interfaces can further modulate the amplitude and the position of the Kiessig fringes.[31] In the case of the destabilized P(S-*b*-MMA) films, the top layer of unanchored P(S-*b*-MMA) lacks interfacial roughness correlation whereas the bottom wetting layer of anchored P(S-*b*-MMA) possesses interfacial roughness correlation.[15] As a result, only the wetting monolayer contributes the fringes in Figure 5. As shown in Figure 11a, the simulation by the IsGISAXS software cannot account for the correlated interfaces and even for the discrepancy in roughness correlation between the two layers in a destabilized thin film.

As shown in Figure 11b, the simulated off-detector-scan profiles reveal a broad hump at 0.1−0.2 Å^{-1} (indicated by a thick arrow) regardless of α_i. In addition, the off-detector-scan profiles reveal oscillations in the vicinity of the hump. An enhancement of the amplitude of oscillations appears as $\alpha_i > \alpha_c^{Si}$. The reason for the enhancement can be explained in terms of the multiple-scattering effect. At low α_i, the multiple scattering events induce a blurring of the sharp interference of oscilations.[12] Once α_i is above the critical angles of the film and substrate, only the two contributions with a similar magnitude over the whole range of exist angles (scattering terms 1 and 2 as illustrated in Figure 1) are dominating the scattering so that the amplitude of oscillations is enhanced.

Furthermore, the amplitude of oscillations/fringes also depends on the size distributions (σ_H and σ_R) of either the thickness H or the base radius R of the cone shape. As shown in Figures 12, increasing σ_R or σ_H induces a blurry of the sharp interference, indicating that the effect of increasing the size distribution is to smooth the off-detector-scan-cut and detector-scan-cut scattering curves.[28] The simulated GISAXS results further verify the speculation of relief structures having a large polydispersive size distribution based on the experimental GISAXS data shown in Figure 7.

Contact Angle and Shape of Relief Structures of P(S-*b*-MMA). We now interpret the physical origin of the contact angle and the shape of relief structures of P(S-*b*-MMA) due to film instability. The contact angle in the range 4−6° measured by AFM is close to the regime of the measured contact angles for polystyrene (PS) melts dewetted from PS brushes, in which the film instability was mainly driven by an entropic effect (i.e., an autophobic behavior).[32] Since an affinity between the PMMA block of P(S-*b*-MMA) and the polar substrate (SiO_x/Si and PMMA−SiO_x/Si) gives rise to a wetting monolayer of P(S-*b*-MMA) brush,[15] the dewetting of P(S-*b*-MMA) thin films on a polar substrate represents that the top layer of unanchored P(S-*b*-MMA) dewetted from the bottom layer of anchored P(S-*b*-MMA). In other words, at the interface between the two layers, the melt of PS blocks autophobically dewetted the brush of PS blocks. Such a behavior is analogous to the dewetting of a PS homopolymer melt on top of a PS homopolymer brush.[32,33] Nonetheless, a quantitative calculation of the contact angle for the autophobic dewetting of a melt of block copolymers on top of a brush of their chemically identical species is not available, but at least we can make an analytic estimation according to the autophobic behavior of a melt of homopolymers on a brush of their chemically identical homopolymers.[34,35] The contact angle of the unanchored P(S-*b*-MMA) on top of the anchored P(S-*b*-MMA) is related to the interfacial tensions between melt-air ($\gamma_{melt\text{-}air}$), brush-air ($\gamma_{brush\text{-}air}$) and brush−melt ($\gamma_{brush-melt}$), as given by the Young's equation:

$$\cos(\theta) = (\gamma_{brush-air} - \gamma_{brush-melt})/(\gamma_{melt-air}) \quad (10)$$

As the chain length is infinite, the surface tension difference between a melt and its brush (i.e., $\gamma_{brush\text{-}air} - \gamma_{melt\text{-}air}$) can be neglected.[36] As a result, the contact angle for the autophobic dewetting of chemically identical species depends on the brush−melt interfacial energy, given by

$$\theta = (2\gamma_{brush-melt}/\gamma_{melt-air})^{1/2} \quad (11)$$

In order to calculate the interfacial energy $\gamma_{brush-melt}$ by the self-consistent field theory (SCFT)[34] and strong segregation theory(SST),[35] the grafting density of a brush has to be known first. The grafting density was calculated using

$$\sigma = \rho d_0 N_A / M_n \quad (12)$$

where d_0 represents the brush height (210 Å by X-ray reflectivity[15]), the mass density of P(S-*b*-MMA) is denoted as ρ (1.08 g/cm^3), and N_A and M_n represent the Avogadro's number and the number-averaged molecular weights of P(S-*b*-MMA), respectively. The P(S-*b*-MMA) monolayer was end-anchored at a density of 0.167 nm^{-2} onto a silicon wafer. According to the grafting density and the other parameters tabulated in Table 1,[37] the brush/melt interfacial tension ($\gamma_{brush-melt}$) of 0.12 dyn/cm was determined by SCFT while $\gamma_{brush-melt} = 0.553$ dyn/cm was obtained based on the calculation by SST.

Given that $\gamma_{brush\text{-}air} = \gamma_{melt\text{-}air} = 27.02$ dyn/cm at 210 °C,[38] the two contact angle values, 5.4° (SCFT) and 11.6° (SST), were estimated, respectively. By comparison, the contact angles, 4−6.5°, experimentally measured by AFM are well in line with the value $\theta = 5.4°$ estimated by SCFT, but deviate from the calculated value based on SST. Although we demonstrate that the experimentally contact angles by AFM are in good quantitative agreement with the prediction by SCFT, one has to note that in practice our experimental conditions deviate from the assumptions made by SST and even by SCFT. First, the measured contact angle might not be an equilibrium angle since the dewetting morphology is holes rather than droplets. Second, the block

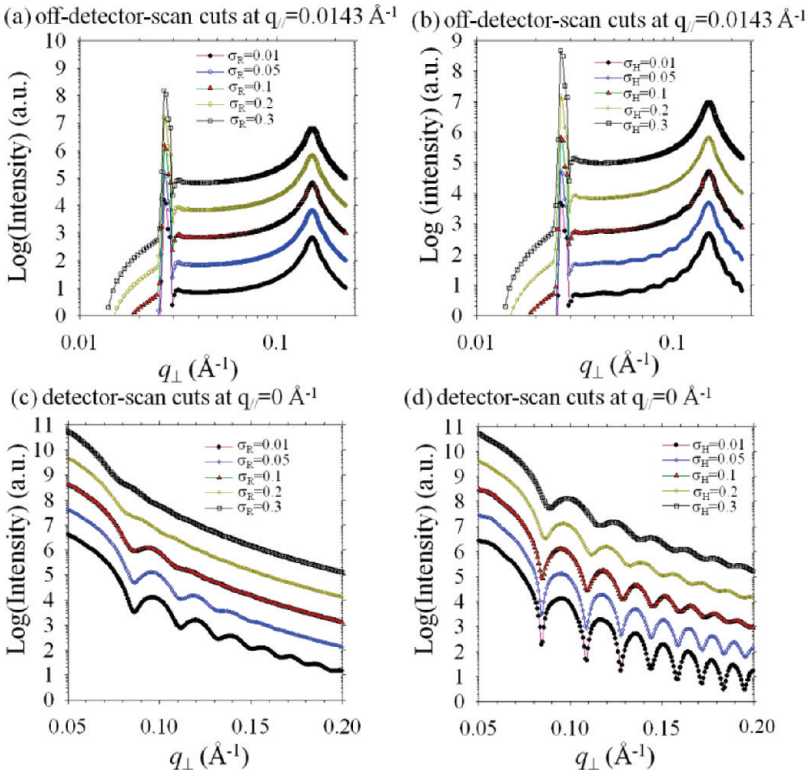

Figure 12. 1D off-detector-scan (the top figures) and detector-scan profiles (the bottom figures) with intensity as a function of $q_\perp$ obtained with vertical cuts at $q_\parallel = 0.0143$ Å^{-1} and $q_\parallel = 0$ Å^{-1} for relief structures between holes having (a, c) various relative widths σ_R of the distribution of a base radius R = 1000 nm (as the hole depth H = 38 nm and its deviation σ_H = 0.2 are fixed), and (b, d) various relative widths σ_H of the distribution of a hole depth H = 38 nm (as the base radius R = 1000 nm and its deviation σ_R = 0.01 are fixed). The grazing incident angle used for simulating the 1D profiles is 0.1875°. The curves were shifted for clarity along the y axis.

Table 1. Parameters for Calculating the Contact Angle by SCFT and SST[a]

quantity	483 K (210 °C)
ρ_0^{-1}	158 Å^3[b]
a	6.91 Å[c]
k_BT (483 K)	6.67×10^{-5} μNÅ
σ	1.67×10^{-3} chains/Å^2
$\sigma N^{1/2}/a\rho_0$ (SCFT)	1.08
$\gamma_{b/h} N^{1/2}/k_BTa\rho_0$ (SCFT)	0.117
$w_\infty/aN^{1/2}$ (SST)	0.4665
$\gamma_{b/h} N^{1/2}/k_BTa\rho_0$ (SST)	0.536
$\gamma_{b/h}$ (SCFT)	0.120 dyn/cm
$\gamma_{b/h}$ (SST)	0.553 dyn/cm

[a] ρ_0^{-1}, a, k_B, σ, N, and w_∞ are respectively, a volume, a statistical length, the Boltzmann constant, the grafting density, the degree of polymerization, and the interfacial width in the limit of infinite chain length. [b] Estimation by $\rho_0^{-1} = f_{PS}\rho_{PS}^{-1} + f_{PMMA}\rho_{PMMA}^{-1}$, in which ρ_{PS}^{-1} and ρ_{PMMA}^{-1} are 165 and 144 Å^3.[37] [c] Estimation by $a = (f_{PS}/a_{PS}^2 + f_{PMMA}/a_{PMMA}^2)^{-1/2}$, in which a_{PS} and a_{PMMA} are 6.7 and 7.5 Å.[37]

copolymer melt is not infinitely long. Third, for simplifying the calculation we ignored the enthalpic effects, such as the interaction $\chi_{PS-PMMA}$ between the PMMA and PS blocks, and affinities at the polymer−substrate and polymer−air interfaces. Because of this assumption, we did not consider the influence of formation of nanostructures within the nonanchored P(S-*b*-MMA) layer on the contact angle. All these uncertainties may lead to inherent discrepancies between the theory and experiment. Nevertheless, the prediction of the SCFT theory indicates that the contact angle of unanchored P(S-*b*-MMA) on the underlying layer of anchored P(S-*b*-MMA) is driven by an autophobic effect.

We now examine the facet-like shape of the relief terraces. The facet-like wedge observed here is similar to the edge shape of large terrace droplets, which have been experimentally observed in symmetric P(S-*b*-MMA) thin films.[39] They found that the terrace P(S-*b*-MMA) droplets formed for thin films having ordered lamellar nanodomains with a parallel orientation with respect to the substrate surface while a spherical cap was observed for the droplet without any internal ordered nanostructures.[39] The faceted droplets have a hyperbolic shape rather than a typically spherical cap for equilibrium droplets. The AFM topographies indicate that the formation of the relief terraces resulted from the autophobic wetting of the unanchored P(S-*b*-MMA) on the monolayer of anchored P(S-*b*-MMA). The top layer of unanchored P(S-*b*-MMA) has one row of PMMA cylindrical nanodomains that parallel oriented to the substrate surface. Thus, the formation of parallel-oriented PMMA cylindrical nanodomains increases the deformation energy, and it will persist to force the shape of relief structures to be a facet-wedge shape.

Conclusion

The GISAXS technique provides much insight into not only ordering but also the spatial orientations of mesophase-separated nanostructures on a substrate, the roughness replication, the thickness of a film and the faceting of microscale-dewetted terraces. The relief terraces formed in destabilized P(S-*b*-MMA) films as a result of thermally induced dewetting on SiO_x/Si and PMMA−SiO_x/Si are due to the incommensurate thickness. According to measurements with an AFM, the nonanchored P(S-*b*-MMA) top layer of the terraces at contact angles in a range 4−6.5° on a monolayer of autophobic P(S-*b*-MMA) brushes anchor onto SiO_x/Si and PMMA−SiO_x/Si. As the P(S-*b*-MMA) terraces have cylindrical PMMA nanodomains preferentially oriented with their long cylindrical axis parallel to the film surface, the terraces with a wedge shape are regarded as faceted

crystals located in the plane of a substrate, consequently producing diffuse scattering streaks in the GISAXS patterns. As GISAXS experiments are performed with a brilliant source—a synchrotron, measurements in situ are practicable to investigate quantitatively the detailed mechanisms of formation of the faceting of relief terraces in destabilized P(S-*b*-MMA) films on annealing with controlled dewetting. Such experiments are in progress.

Acknowledgment. National Science Council provided support (NSC 97-2218-E-008-011-MY2). We thank Dr. U-Ser Jeng, Dr. Chiu-Hun Su, and Dr. Chun-Jen Su for their assistance with the GISAXS experiments at NSRRC beamline BL23A, and Dr. Pin-Jiun Wu for his discussion of X-ray reflectivity data at NSRRC.

References and Notes

(1) Limary, R.; Green, P. F. *Langmuir* **1999**, *15*, 5617–5622.
(2) Limary, R.; Green, P. F. *Macromolecules* **1999**, *32*, 8167–8172.
(3) Masson, J. L.; Limary, R.; Green, P. F. *J. Chem. Phys.* **2001**, *114*, 10963–10967.
(4) Coulon, G.; Russell, T. P.; Deline, V. R.; Green, P. F. *Macromolecules* **1989**, *22*, 2581–2589.
(5) Anastasiadis, S. H.; Russell, T. P.; Satija, S. K.; Majkrzak, C. F. *Phys. Rev. Lett.* **1989**, *62*, 1852–1855.
(6) Henkee, C. S.; Thomas, E. L.; Fetters., L. J. *J. Mater. Sci.* **1988**, *23*, 1685–1694.
(7) Tsarkova, L.; Knoll, A.; Krausch, G.; Magerle, R. *Macromolecules* **2006**, *39*, 3608–3615.
(8) Park, I.; Park, S.; Park, H. W.; Chang, T.; Yang, H. C.; Ryu, C. Y. *Macromolecules* **2006**, *39*, 315–318.
(9) Harrison, C.; Park, M.; Chaikin, P.; Register, R. A.; Adamson, D. H.; Yao, N. *Macromolecules* **1998**, *31*, 2185–2189.
(10) Lee, B.; Park, I.; Yoon, J.; Park, S.; Kim, J.; Kim, K. W.; Chang, T.; Ree, M. *Macromolecules* **2005**, *38*, 4311–4323.
(11) Lazzari, R. *J. Appl. Crystallogr.* **2002**, *35*, 406–421.
(12) Renaud, G.; Lazzari, R.; Leroy, F. *Surf. Sci. Rep.* **2009**, *64*, 255–380.
(13) Ji, S. X.; Liu, G. L.; Zheng, F.; Craig, G. S. W.; Himpsel, F. J.; Nealey, P. F. *Adv. Mater.* **2008**, *20*, 3054–3060.
(14) Jeng, U. S.; Su, C. H.; Su, C. J.; Liao, K. F.; Chuang, W. T.; Lai, Y. H.; Chang, J. W.; Chen, Y. J.; Huang, Y. S.; Lee, M. T.; Yu, K. L.; Lin, J. M.; Liu, D. G.; Chang, C. F.; Liu, C. Y.; Chang, C. H.; Liang, K. S. *J. Appl. Crystallogr.* **2010**, *43*, 110–121.
(15) Sun, Y. S.; Chien, S. W.; Wu, P. J. *Macromolecules* **2010**, *43*, 5016−5023.
(16) von Laue, M. *Ann. Phys.* **1936**, *26*, 55–85.
(17) Richard, M. I.; Schülli, T. U.; Renaud, G.; Wintersberger, E.; Chen, G.; Bauer, G.; Holý, V. *Phys. Rev. B* **2009**, *80*, 045313−1–045313−9.
(18) Vartanyants, I. A.; Zozulya, A. V.; Mundboth, K.; Yefanov, O. M.; Richard, M. I.; Wintersberger, E.; Stangl, J.; Diaz, A.; Mocuta, C.; Metzger, T. H.; Bauer, G.; Boeck, T.; Schmidbauer, M. *Phys. Rev. B* **2008**, *77*, 115317−1–115317−9.
(19) Narayanan, S.; Lee, D. R.; Guico, R. S.; Sinha, S. K.; Wang, J. *Phys. Rev. Lett.* **2005**, *94*, 145504−1–145504−4.
(20) Müller-Buschbaum, P.; Gutmann, J. S.; Lorenz, C.; Schmitt, T.; Stamm, M. *Macromolecules* **1998**, *31*, 9265–9272.
(21) Müller-Buschbaum, P.; Stamm, M. *Macromolecules* **1998**, *31*, 3686–3692.
(22) Lambooy, P.; Russell, T. P.; Kellogg, G. J.; Mayes, A. M.; Gallagher, P. D.; Satija, S. K. *Phys. Rev. Lett.* **1994**, *72*, 2899–2902.
(23) Koneripalli, N.; Singh, N.; Levicky, R.; Bates, F. S.; Gallagher, P. D.; Satija, S. K. *Macromolecules* **1995**, *28*, 2897–2904.
(24) Mansky, P.; Russell, T. P.; Hawker, C. J.; Pitsikalis, M.; Mays, J. *Macromolecules* **1997**, *30*, 6810–6813.
(25) Stein, G. E.; Lee, W. B.; Fredrickson, G. H.; Kramer, E. J.; Li, X.; Wang, J. *Macromolecules* **2007**, *40*, 5791–5800.
(26) Hammond, M. R.; Cochran, E.; Fredrickson, G. H.; Kramer, E. J. *Macromolecules* **2005**, *38*, 6575–6585.
(27) Müller-Buschbaum, P.; Schulz, L.; Metwalli, E.; Moulin, J. F.; Cubitt, R. *Langmuir* **2008**, *24*, 7639–7644.
(28) Revenant, C.; Leroy, F.; Lazzari, R.; Renaud, G.; Henry, C. R. *Phys. Rev. B* **2004**, *69*, 035411−1−035411−17.
(29) Roe, R. J. *Methods of X-ray and Neutron Scattering in Polymer Science*; Oxford University Press: New York, 2000; Chapter 5 and references therein.
(30) Shin, K.; Pu, Y.; Rafailovich, M. H.; Sokolov, J.; Seeck, O. H.; Sinha, S. K.; Tolan, M.; Kolb, R. *Macromolecules* **2001**, *34*, 5620–5626.
(31) Kaganer, V. M.; Stepanov, S. A.; Kohler, R. *Phys. Rev. B* **1995**, *52*, 16369–16372.
(32) Reiter, G.; Auroy, P.; Auvray, L. *Macromolecules* **1996**, *29*, 2150–2157.
(33) Liu, Y.; Rafailovich, M. H.; Sokolov, J.; Schwarz, S. A.; Zhong, X.; Eisenberg, A.; Kramer, E. J.; Sauer, B. B.; Satija, S. *Phys. Rev. Lett.* **1994**, *73*, 440–443.
(34) Matsen, M. W.; Gardiner, J. M. *J. Chem. Phys.* **2001**, *115*, 2794–2804.
(35) Likhtman, A. E.; Semenov, A. N. *Europhys. Lett.* **2000**, *51*, 307–313.
(36) Leibler, L.; Ajdari, A.; Mourran, A.; Coulon, G.; Chatebay, D. In *Ordering in Macromolecules Systems*; Teramoto, A., Kobayashi, M., Norisuje, T., Eds.; Springer-Verlag: Berlin, 1994; pp 301−311.
(37) Shull, K. R.; Mayes, A. M.; Russell, T. P. *Macromolecules* **1993**, *26*, 3929–3936.
(38) Wu, S. *J. Phys. Chem.* **1970**, *74*, 632–638.
(39) Croll, A. B.; Massa, M. V.; Matsen, M. W.; Dalnoki-Veress, K. *Phys. Rev. Lett.* **2006**, *97*, 204502–1−204502−4.